

Panopticon: Advancing Any-Sensor Foundation Models for Earth Observation

Leonard Waldmann^{1,2*} Ando Shah^{1*} Yi Wang² Nils Lehmann² Adam J. Stewart²
 Zhitong Xiong² Xiao Xiang Zhu² Stefan Bauer² John Chuang¹

¹University of California, Berkeley; ²Technical University of Munich
 correspondence to ando@berkeley.edu

Abstract

Earth observation (EO) data features diverse sensing platforms with varying spectral bands, spatial resolutions, and sensing modalities. While most prior work has constrained inputs to fixed sensors, a new class of any-sensor foundation models able to process arbitrary sensors has recently emerged. Contributing to this line of work, we propose Panopticon, an any-sensor foundation model built on the DINOv2 framework. We extend DINOv2 by (1) treating images of the same geolocation across sensors as natural augmentations, (2) subsampling channels to diversify spectral input, and (3) adding a cross attention over channels as a flexible patch embedding mechanism. By encoding the wavelength and modes of optical and synthetic aperture radar sensors, respectively, Panopticon can effectively process any combination of arbitrary channels. In extensive evaluations, we achieve state-of-the-art performance on GEO-Bench, especially on the widely-used Sentinel-1 and Sentinel-2 sensors, while out-competing other any-sensor models, as well as domain adapted fixed-sensor models on unique sensor configurations. Panopticon enables immediate generalization to both existing and future satellite platforms, advancing sensor-agnostic EO.

1. Introduction

Earth observation (EO) satellites provide essential data for monitoring our planet, from detecting illegal mining [49] and dark vessels [40], to field delineation [23] and yield prediction [44]. Recent years have witnessed substantial progress towards remote sensing foundation models (RSFMs) that have adapted computer vision methods designed for RGB imagery to EO data [11, 38, 43, 62]. However, compared to natural images, remote sensing data is remarkably heterogeneous [45, 52, 54]. EO platforms gen-

erate tremendously varied data across multiple dimensions, including spatial resolution (centimeters to kilometers), spectral characteristics (multispectral, hyperspectral, radar), revisit times (continuous to static), swath widths, preprocessing levels (raw, top of atmosphere, surface reflectance), and sensing mechanisms (active vs. passive). While RSFMs began as sensor-specific models [11, 21, 30, 47, 58], the current trend is towards more flexible models that can deal with a variety of EO data [1, 13, 29, 50, 61, 65].

Most recently, an emerging class of any-sensor models has begun addressing the fundamental challenge of sensor agnosticism in EO. With only a few examples at the time of writing [42, 64], these models process data from arbitrary sensor configurations—including unseen combinations of spectral bands, resolutions, and modalities—without requiring sensor-specific adaptations during inference. They achieve this by decoupling spectral and spatial processing while incorporating knowledge of sensor-specific properties such as spectral response functions (SRFs) and ground sampling distances (GSDs).

In this work, we propose Panopticon, a new any-sensor model (see supplementary material for the etymology of this name). Building upon the DINOv2 [39] framework, we make three key modifications for stronger integration of satellite data as a distinct data modality [45]. First, instead of distilling knowledge within a single image, we regard a given geolocation or “footprint” as an object of interest and consider snapshots from different sensors of that footprint as different views of the same object. This approach enables us to sample a broad spectrum of natural sensor-to-sensor variation by incorporating images from different channel characteristics, modalities, timestamps, and processing levels. Second, in addition to standard DINOv2 spatial augmentations, we apply spectral augmentations through channel sub-sampling or spectral cropping for multispectral (MS), hyperspectral (HS), and synthetic aperture radar (SAR) data. Third, to handle views with varying numbers of channels, we implement a cross-attention over channels with added positional embeddings that encode sensor-specific spectral information into a unified rep-

* Denotes co-first authorship, ordered randomly. Co-first authors will prioritize their names on their resumes/websites

Code: <https://github.com/Panopticon-FM/panopticon>

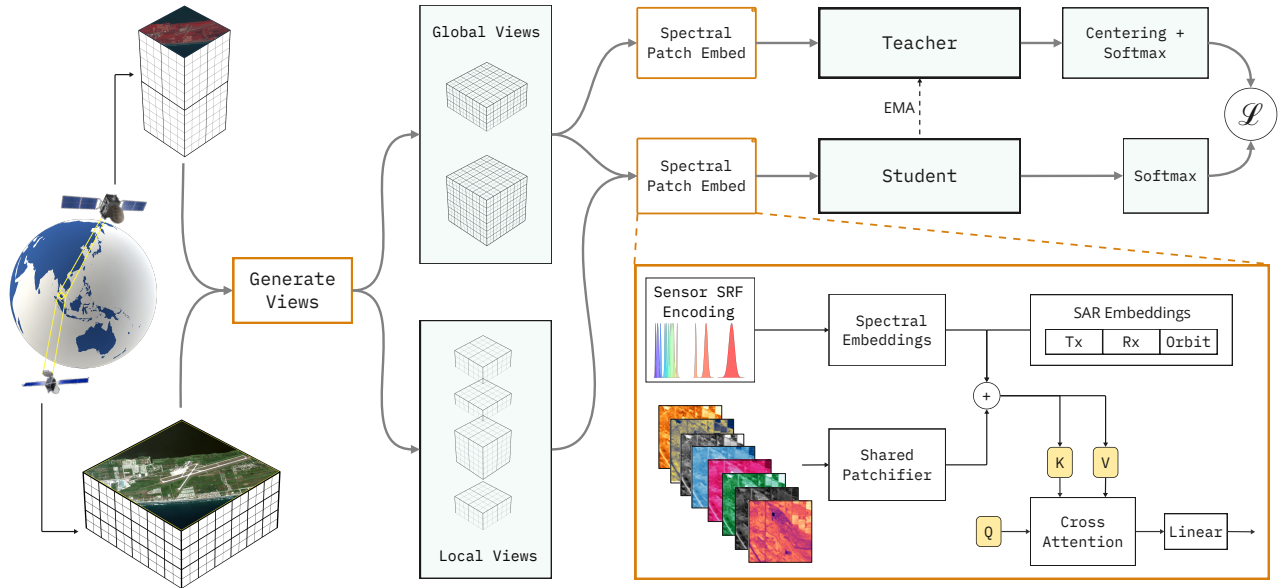


Figure 1. Architecture of Panopticon. The highlighted blocks indicate our modifications to the DINOv2 framework. Images of the same geographic footprint, as captured by different sensors at different times, scales, etc. are used to generate multiple views of this object. The spectral patch embedding block uses a shared patchifier to tokenize incoming views and a cross attention to efficiently fuse tokens across channels. The student branch has to predict coarse and fine-grain representations from an information-poor view, relative to the teacher’s information-rich view, using an exponential moving average (EMA).

resentation.

To evaluate spectral flexibility, we simulate new sensors from HS datasets using spectral convolution [5], and subject models to reduced spectral and scale information to assess their invariance to these properties, in addition to assessing performance on sensors not encountered during pre-training. We demonstrate that Panopticon also achieves state-of-the-art performance on GEO-Bench [27] which comprises of popular sensors such as Sentinel-1 (S1) and Sentinel-2 (S2). To address sensor distribution shifts in fixed-sensor models, we employ patch embedding re-training [4, 19] to overcome channel incompatibility issues, achieving parameter-efficient domain adaptation. A surprising finding is that DINOv2 serves as a remarkably strong baseline in these comparisons, hinting at the nature of future work. Through comprehensive experiments across 22 MS, HS, and SAR datasets, we provide valuable insights into the capabilities and limitations of current approaches to sensor-agnostic learning in EO.

In summary, our contributions are as follows:

- We introduce Panopticon, a RSFM capable of building representations for any MS, HS, or SAR sensor, regardless of GSD or spectral characteristics.
- While maintaining competitive-to-state-of-the-art performance on established benchmarks, Panopticon outperforms other any-sensor models on more unique sensor configurations that cover important application domains.

- We find that spectral progressive pre-training combined with a wider embedding dimension and the use of spectral embeddings in the channel attention module are crucial for optimal performance.

2. Related work

Fixed-sensor RSFMs Approaches vary on how to process different sensors with the same model. USat [20] and msGFM [16] use sensor-specific patch embeddings feeding into a single encoder, with USat adding positional information to tokens. SatMAE [11], Galileo [51], and AnySat [1] employ more granular approaches with patch embeddings for channel groups. Video-inspired models like Prithvi [22] and schoS2MAE [29] patchify in spatio-temporal or spatio-spectral dimensions. Another line of work uses separate encoders and aligns the resulting sensor-specific representations through contrastive loss, as in CROMA [13], modified contrastive loss, as in IAI-SimCLR [41], or regularization of covariance matrices, as in DeCUR [60].

Any-sensor RSFMs To the best of our knowledge, two general-purpose any-sensor models have been proposed, both based on the MAE [17] architecture. DOFA [64] proposes dynamic weight generation based on wavelengths of the input channels for the otherwise fixed-shaped input projection and final layer of the decoder. SenPa-MAE [42]

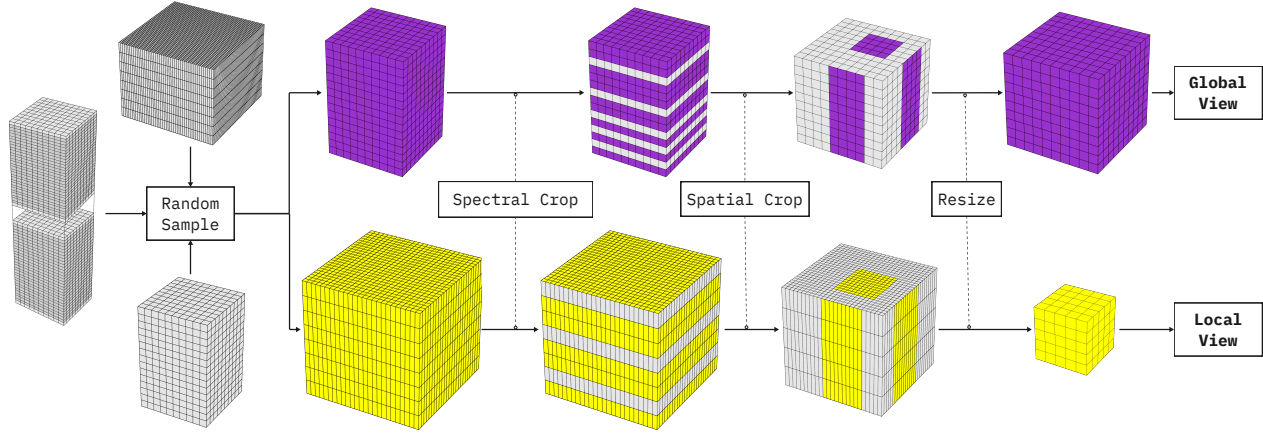


Figure 2. View Generation. Given a footprint, we randomly sample a snapshot performing an implicit spectral augmentation. To increase spectral variance, we apply a spectral crop, and following DINOv2, we apply a spatial crop and resize to generate the final view. Local and global views are created similarly but with different augmentation parameters to ensure information-rich global and information-poor local views.

patchifies each channel separately with the same projection and adds both positional and spectral embeddings¹ based on the spectral response function (SRF) of the channel to the tokens in the encoder and decoder.

Temporal and spectral augmentations Several RSFMs have utilized the naturally occurring temporal and spectral differences between footprints as augmentations. In particular, DINO-MC [63] uses temporal positive pairs, SeCo [34] incorporates seasonal differences into their branches, and CaCo [32] defines change-aware positive and negative temporal pairs. On the other hand, DINO-MM [57] randomly selects different sensors for each view as a spectral augmentation. Finally, A2MAE [66] applies meta-info-aware masking to generate both spectrally and temporally varied tokens.

DINOv2 DINO [6] uses a multi-view approach with global and local views processed by teacher and student networks. The teacher uses momentum encoding and applies centering and sharpening to prevent mode collapse, while the student learns from these outputs. This approach enables models to learn viewpoint and scale-invariant features through self-distillation. DINOv2 [39] extends DINO by incorporating the patch-wise iBOT loss [67] and scaling training. Importantly, a ViT-B DINOv2 checkpoint distilled from a large ViT-giant run is available.

3. Method

We propose Panopticon, which builds on the DINOv2 architecture and training framework [39] with changes to view

¹as well as gsd encoding.

generation and patch embedding. In this section, we describe our approach in detail.

3.1. Sensors as views of a geographic footprint

A major component of the DINO framework is distilling knowledge from information-rich to information-poor views of the same object. In particular, DINO uses an image as object with large and small spatial crops as views. Instead of considering a single image as the object of interest, we consider a geographic footprint as the object of interest and treat images from different sensors as spectral views and therefore augmentations of the same object. These snapshots not only vary in spectral configuration but also in GSDs, acquisition time, and processing levels (as shown in Table 1), allowing our model to distill diverse information across sensors. For a given footprint, we obtain n differently shaped snapshots $\mathcal{X} = \{c_i \times h_i \times w_i\}_{i=1\dots n}$.

3.2. Local and global view generation

Let us first generate a local view from the available snapshots \mathcal{X} . We start by selecting a snapshot $x \in \mathcal{X}$ whereby we implicitly apply a temporal and spectral augmentation to our geolocation. Since the number of unique sensors in the training dataset is limited in practice, we increase the variance of the spectral information by subsampling channels. In particular, we first sample the number of channels $c \in \{c_{\text{low}}^L, \dots, c_{\text{high}}^L\}$ and then select c unique channels from x . Images with $c < c_{\text{low}}^L$ are not subsampled. All sampling is done uniformly at random. As in DINO, we apply a random resize crop resizing to the spatial shape $W^L \times H^L$. In summary, we select a view, apply spectral cropping, spatial augmentations, and finally resize, c.f. Fig. 2. We repeat this process to generate n_L local views. Analogously, we gen-

Dataset	Locations	Sensors	GSD (m)	Footprint (km ²)	Sensor Modalities (# bands)	Temporal Range	Processing Level
fMoW [8, 11]	90K	QB, GE, WV2/3, S2	0.3–10	0.2–25	RGB (3), MS (4, 8, 12)	2002–2020	L2A
MMEarth [36]	1.2M	S1, S2	10	1.7	SAR (8), MS (12)	2017–2020	L1C, L2A
SatlasPretrain [3]	770K	S1, S2, L9	10–100	25	SAR (2), MS (9), Thermal (2)	2022	L1C
SpectralEarth [4]	538K	EnMAP	30	14.7	HS (202)	2022–2024	L2A

Table 1. Pretraining datasets for Panopticon. fMoW refers to the combined fMoW-full and fMoW-Sentinel datasets. Locations refers to the number of unique footprints, where footprint sizes are shown in square kilometers. The parentheses around values indicates the number of channels for that modality. QB = QuickBird-1, GE = GeoEye-2, WV = WorldView, S1 = Sentinel-1, S2 = Sentinel-2, and L9 = Landsat 9.

erate n_G global views with parameters $c_{\text{low}}^G, c_{\text{high}}^G, W^G, H^G$. In correspondence with DINOv2, we set $n^L = 4, n^G = 2, H^L = W^L = 96$, and $H^G = W^G = 224$. To be able to fit a full S2 image into a global crop, we set $c_{\text{high}}^G = 13$ and for maximum flexibility, we set $c_{\text{low}}^L = 1$. Similarly to the scales in the DINO random resized crop, we finally set $c_{\text{high}}^L = c_{\text{low}}^G = 4$ to correspond to roughly $1/3 \approx 4/13$ of the full information, c.f. Sec. F. Overall, we obtain global views $\{c_i^G \times H^G \times W^G\}_{i=1, \dots, n^G}$ and local views $\{c_i^L \times H^L \times W^L\}_{i=1, \dots, n^L}$.

3.3. Attention over channels as patch embedding

Since our views have different numbers of channels, we cannot use the standard 2D convolution as patch embedding. Instead, we use a cross attention over input channels where the positional embeddings encode spectral information of the channels as proposed by Nguyen et al. [37]. Let $\{c_i \times H \times W\}_i$ be our input to the patch embedding (PE). We first apply the *same* 2D convolution to each individual channel to obtain $\{c_i \times P \times P \times D_{\text{attn}}\}_i$, where P is the patch size. We abstract away the spatial dimension and use $\{P^2 \times c_i \times D_{\text{attn}}\}_i$ as keys and values for a cross attention with a learned query $1 \times 1 \times D_{\text{attn}}$. This reduces arbitrary channel dimensions $\{c_i\}_i$ to a tensor of fixed size $P^2 \times 1 \times D_{\text{attn}}$. Reshaping and a linear projection finally yields $P^2 \times D_{\text{out}}$. We implement the initial PE with a $1 \times P \times P$ 3D convolution as in Bao et al. [2] and employ padding and masking to effectively calculate the cross attention for batched inputs. From here, the standard DINOv2 pipeline continues.

To ingest spectral information about the individual channels, we add the following embeddings to keys and values of the cross attention. For optical channels, we choose the standard positional encoding [56] at the position equal to the mean wavelength λ of the channel in nanometers (e.g., 664 nm for red), i.e.

$$\text{PE}_{(\text{pos}, 2i)} = \sin(\omega_i \lambda), \quad (1)$$

$$\text{PE}_{(\text{pos}, 2i+1)} = \cos(\omega_i \lambda), \quad (2)$$

where $\omega_i = \frac{1}{10000^{2i/D_{\text{attn}}}}$. We categorize SAR channels into 8 categories based on their orbit direction (i.e. ascending, descending) and transmit and receive polarizations (i.e. vertical, horizontal for each). We learn embeddings of dimension $d_{\text{attn}}/3$ for each and concatenate them for the full embedding vector. This follows the results from the literature that SAR data generated across polarizations [10, 53] and orbits [31, 54] are known to be distinct. Note that we only infuse spectral information but no information on GSD, time, or processing levels.

3.4. Spectral progressive pre-training

We found that naively training Panopticon with diverse sensors yields poor performance. Inspired by sample progressive pre-training [35, 64], we pretrain in multiple stages gradually increasing the sensor diversity. In Sec. 5, we show that this simple choice substantially increase performance in as few as two stages.

3.5. Implementation details

Datasets We use the datasets presented in Tab. 1 with the following rationale:

- **fMoW**, comprising of fMoW [8] and fMoW-Sentinel [11], combines popular optical wavelengths (RGB, S2) and commercial MS sensors - WorldView (WV) 2/3, with high variation in GSD and high resolution RGB images.
- **SatlasPretrain** [3] allows distillation between paired S1 SAR, S2 optical, and Landsat 9 optical and thermal sensors across globally diverse footprints.
- **MMEarth** [36] provides additional SAR configurations—ascending and descending orbits with VV, VH, HV, and HH polarizations not found in other datasets.
- **SpectralEarth** [4] allows distillation between a wide spectrum of HS optical wavelengths.

Each dataset is standardized with mean and standard deviations computed over its training split. All datasets are implemented using the TorchGeo library [48]. Additional

	Commercial Sensors		Synthesized Sensors				OOD Sensors	
	SpaceNet1 WV7	FMoW-10% WV8	Corine SuperDove	Corine MODIS	Hyperview SuperDove	Hyperview MODIS	TC-10% GOES-16	DT-10% Himawari
	mIoU (%) \uparrow	Acc (%) \uparrow	mAP (%) \uparrow	mAP (%) \uparrow	MSE \downarrow	MSE \downarrow	MSE \downarrow	MSE \downarrow
DINOv2-PE	90.0	29.2 / <u>47.0</u> *	66.8	63.6	1.043	0.639	0.635	0.502
Croma-PE	89.4	33.7	70.5	72.2	0.343	0.519	0.394	0.925
Softcon-PE	<u>90.1</u>	32.8	<u>70.9</u>	<u>72.6</u>	0.353	0.533	0.471	<u>0.810</u>
Anysat-PE	87.7	26.2	68.9	70.7	<u>0.326</u>	-	0.449	1.406
SenPaMAE	86.2	16.9	59.5	60.1	0.366	0.355	-	-
DOFA	89.9	42.0	63.9	65.8	0.334	<u>0.338</u>	<u>0.385</u>	1.032
Panopticon	90.3	50.3	85.8	86.2	0.313	0.321	0.315	0.963

Table 2. Spectral generalization performance. Synthesized sensor channels are generated from EnMAP source bands using spectral convolution to indicated target sensors, and tested on the SpectralEarth Corine dataset using 10% of the training set. Similarly, the Intuition-1 HS sensor is transformed to target bands for the Hyperview dataset. Target bands are generated through spectral convolution for Planet SuperDove’s (SD) 8 bands, or MODIS Terra’s 16 bands. Out-of-distribution (OOD) sensors refer to weather satellite channels with central wavelengths of 10.4 μm . Missing cells indicate the inability of models to adapt to those settings. Best performers are **bolded** and second-best underlined. *Trained re-initialized PE / frozen pre-trained PE using only RGB channels. DT = DigitalTyphoon and TC = TropicalCyclone.

	Classification (top-1 Accuracy %) \uparrow						Segmentation (mIOU %) \uparrow			
	BENV2-10%		m-eurosat	m-forestnet	m-so2sat	RESISC45	m-sacrop	m-cashew	m-nzcattle	m-pv4ger
	S2	S1	S2	L8	S2	RGB	S2	S2	RGB	RGB
DINOv2	80.1	-	<u>95.5</u>	<u>53.5</u>	<u>60.8</u>	94.0	51.2	65.9	<u>92.7</u>	96.9
CROMA	79.4	70.3	91.1	-	53.5	-	48.4	44.3	-	-
SoftCon	84.3	80.0	92.2	-	52.1	-	<u>51.3</u>	54.5	-	-
AnySat	76.8	64.4	87.6	50.9	42.5	65.5	39.5	38.8	92.5	92.2
Galileo	76.5	70.3	88.6	-	54.2	-	39.5	40.4	-	-
SenPaMAE	63.8	-	77.5	33.5	33.7	28.2	39.3	40.7	89.5	78.3
DOFA	78.8	72.0	92.9	53.2	54.2	92.0	<u>51.3</u>	56.4	92.8	<u>96.3</u>
Panopticon	<u>83.9</u>	<u>78.4</u>	96.4	56.3	61.7	<u>90.9</u>	52.6	<u>59.3</u>	92.6	95.2

Table 3. Classification and segmentation on datasets consisting of well-known sensors from GEO-Bench, BENV2, and RESISC45. A ‘-’ indicates the inability of the model to process the dataset at hand. As baseline we report the vanilla pre-trained DINOv2 weights only using RGB channels from the respective dataset. Interestingly, this constitutes a very strong baseline. Panopticon is in the top 2 models for all but 2 tasks. Best performers are **bolded** and second-best underlined.

details are available in the supplementary section.

Model and DINOv2 pre-trained weights We use a ViT-B and load the official DINOv2 weights. However, weights for the classification and iBOT heads are not publicly available and random initialization of these components led to training instability. Hence, we first fine-tune the provided DINOv2 weights on the RGB channels of the fMoW dataset until convergence and use those head weights for initialization of Panopticon. This approach provided stable training dynamics for our model.

Training configuration We train our model in two stages using only fMoW in the first stage and all datasets in the second stage, c.f. Sec. 5. Following DINOv2, we artificially define an epoch as 1250 iterations and train for 87.5K iterations or 70 epochs on 16 A100 40GB GPUs with an effective batch size of 1200. Further details can be found in the supplementary materials.

4. Evaluation

We evaluate our model against DINOv2, many-sensor models, and any-sensor models in linear probing and k NN settings for 11 classification, 7 segmentation, and 4 regres-

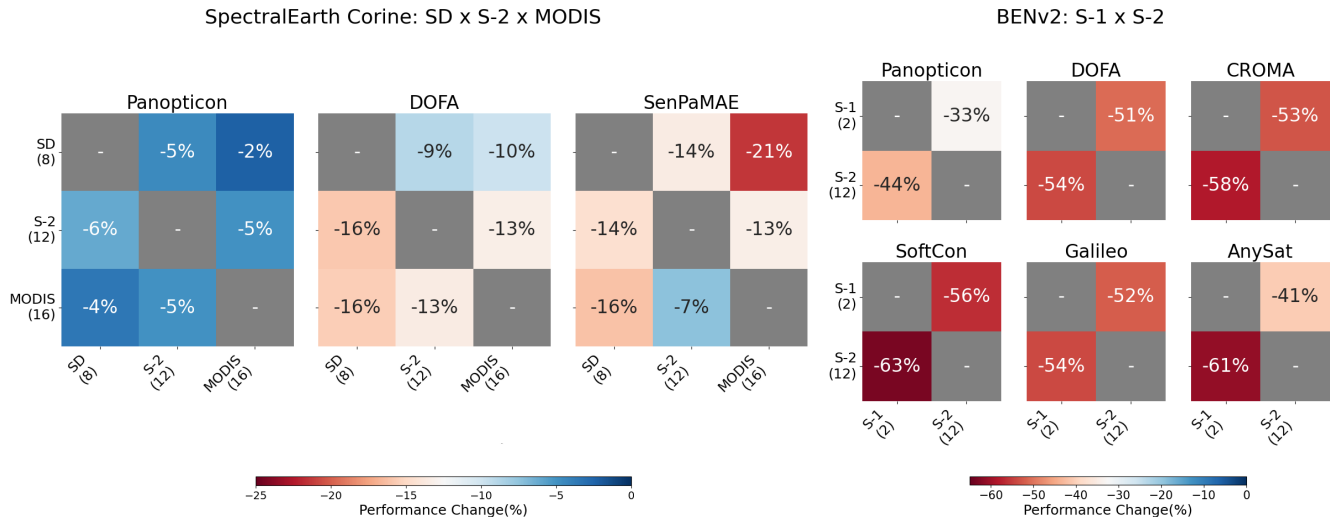


Figure 3. Cross-sensor invariance. In addition to train/val/test splits, we also split datasets across sensors to explicitly test sensor invariance. y -axes on the heatmap represent training sensors and x -axes, test sensors. The diagonals represent same-sensor for train and test, and are grayed-out, while off-diagonal elements represent cross-sensor results with values expressed as percentage differences from the diagonals. This enables visualization of the change in cross-sensor performance relative to same sensor, expressed in (negative) percentages. **Left:** splits are across synthesized sensors from the HS EnMAP sensor using spectral convolution - MODIS, Sentinel-2 and Planet SuperDove, for any-sensor models. **Right:** BigEarthNet-v2; splits are implemented across Sentinel-1 and Sentinel-2 sensors, for all any-sensor and many-sensor models, except SenPaMAE which cannot process SAR imagery. Panopticon consistently outperforms other cross-sensor settings. Note that the value ranges differ for the two sub-figures.

sion downstream tasks. We evaluate sensor generalization in two specific ways: a) the ability to generalize to unseen sensor configurations, and b) the ability to generate representations that are scale and spectrally invariant. We test performance on commonly utilized EO benchmarks such as GEO-Bench [27]. All evaluation is conducted on the **VIT-Base** model only against models of comparable sizes.

4.1. Generalization to unique sensors

We evaluate Panopticon against state-of-the-art (SOTA) any-sensor and many-sensor models on datasets with sensor configurations that were not explicitly encountered during pre-training. Given the limited availability of open-access data and benchmarks from commercial sensors [46], we employ spectral convolution over hyperspectral (HS) bands to simulate existing sensors with different spectral characteristics; additional details in the supplementary materials. Using the SpectralEarth-Corine dataset [4], we transform the HS bands to correspond with Planet’s SuperDove sensor (8 bands) and MODIS Terra sensor (16 bands), creating the ① Corine-SD and ② Corine-MODIS datasets, respectively. We apply the same transformation to the Hyperview [26] HS dataset, mapping it to ③ SuperDove and ④ MODIS bands. Finally we employ the wind speed estimation tasks ⑤ TropicalCyclone [33] and ⑥ Digital-Typhoon [25] for their extreme spectral distribution shifts with wavelengths of 10.4 μm . For any-sensor models with

fixed channel dimensions, we implement patch embedding module retraining while keeping the backbone frozen, denoted by the suffix “-PE”. This approach has shown to be a parameter-efficient domain adaptation strategy for EO foundation models [19]. This methodology enables comparison of sensor generalization capabilities across a diverse range of models using valuable but difficult-to-access sensor configurations. Additionally, we include benchmarks datasets that contain two commercial sensors: ⑦ SpaceNet 1 [55] which uses the WV2 sensor, and the ⑧ fMoW dataset that includes only the WV2+WV3 sensors (10%).

Table 2 summarizes the results. While the domain adapted fixed-sensor models work well and often outperform previous any-sensor models, Panopticon almost uniformly excels at these tasks, in most cases by a substantial margin.

4.2. Sensor invariance

We explicitly test for a model’s ability to generate stable representations regardless of the sensor input. To do this, we implement an additional split dimension on datasets that have paired sensors. We use the ⑩ EnMAP-Corine [4] dataset where we employ spectral convolution to simulate MODIS, Sentinel-2, and Planet SuperDove sensors (Fig. 3 (left)) and the ⑫ BigEarthNet-v2 [9] dataset that has paired imagery from Sentinel-1 and Sentinel-2 (Fig. 3 (right)). Models are trained on the training split of the dataset us-

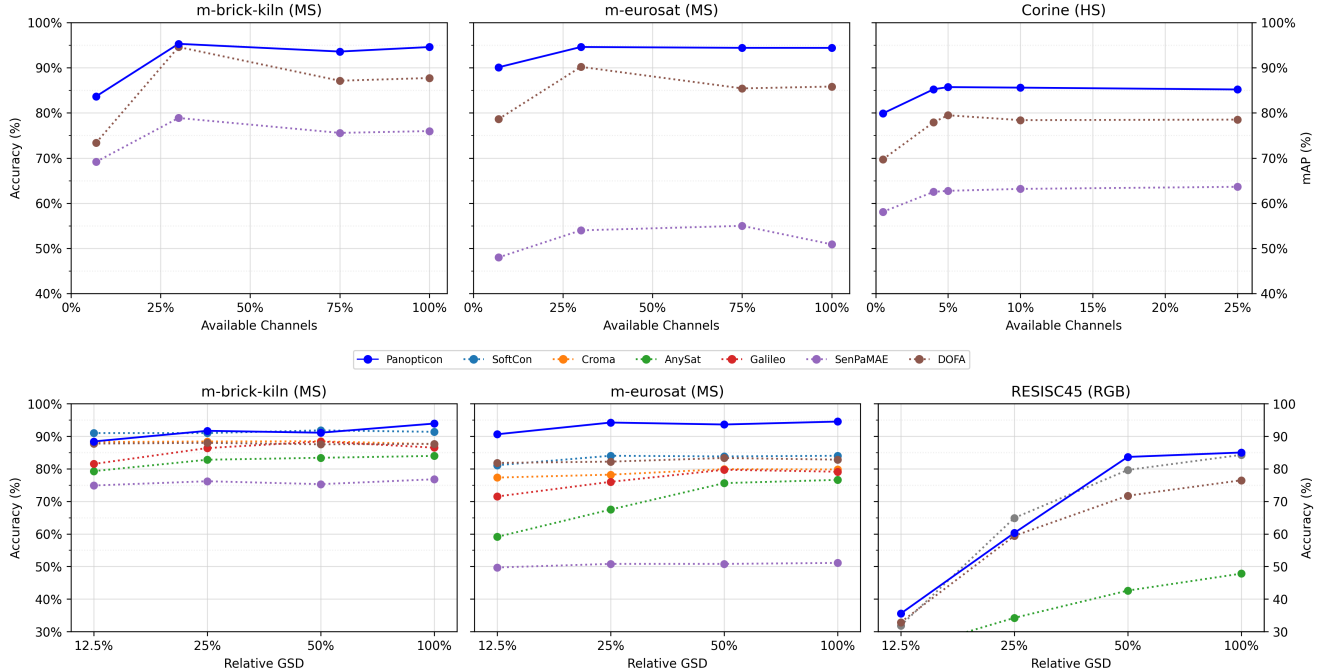


Figure 4. Representation stability across sensing conditions. **Top:** Learning stable representations under spectral subsampling. Representations generated by Panopticon remain more stable and perform better than the state of the art in any-sensor models, as spectral information is reduced. For MS tasks m-eurosat and m-brick-kiln (left), we randomly subsample the number of available channels and assess k NN top-1 accuracy, setting $k = 20$. For the HS land cover prediction task (right) for EnMAP-Corine, we conduct the same procedure, with linear probing. **Bottom:** Learning scale-invariant representations. Representations generated by Panopticon remain more stable and perform better than the state of the art in many-sensor, any-sensor, and DINOv2 baseline. Panopticon is shown as a dark blue solid line in all plots.

ing a single sensor, while being validated and tested on a corresponding split of the dataset, using data from a different sensor. We then plot the relative difference to the same-sensor setting as shown on the off-diagonal cells. This allows us to validate how close representations generated from one sensor are to ones generated from a different sensor on the same dataset and prediction objective. Ideally, the off-diagonal cell values are close to 0%, i.e. similar to the same-sensor setting. This is the case for Panopticon for the Corine dataset in Fig. 3 (left), where other any-sensor models struggle to generalize, especially when training on fewer bands (SD with 8 bands) and testing on sensors with more bands (MODIS with 16 bands). This effect is less pronounced in Fig. 3 (right), where the domain shift is very strong going from optical to SAR and vice-versa. However, even in this setting Panopticon outperforms all any-sensor and many-sensor models by 18% and 14%, for the $S1 \rightarrow S2$ and $S2 \rightarrow S1$ settings on average, respectively.

Absolute values for these experiments along with additional results on the fMoW dataset split according to three included sensors, can be seen in Supplementary Fig. 7.

4.3. Spectral invariance

In this section we approach spectral invariance as a function of available spectral channels in optical MS imagery. Inspired by the methodology of Reed et al. [43], we evaluate spectral invariance by progressively reducing the number of available spectral channels while measuring model performance degradation, as illustrated in Fig. 4 (top). We do this by randomly subsampling the available channels for a given dataset². This assessment employs k -nearest neighbors (k NN) classification on two MS datasets: ⑧ EuroSAT [18] and ⑨ Brick Kiln [28], both modified according to GEO-Bench specifications [27]. For the HS ⑩ EnMAP-Corine dataset [4], we implement linear probing (LP) for multilabel land cover classification. We evaluate only any-sensor models as they alone can process arbitrary channels without modification, revealing their inherent spectral representation quality.

Panopticon retains the ability to generate high quality representations across almost the entire range of spectral subsampling, exhibiting high spectral invariance within

²For MS, we sample b channels uniformly at random identically for each model. For HS, we bin the channel range into equal sized bins, b and sample uniformly at random within bins, again keeping the choices fixed across models. $b_{HS} \in \{1, 4, 10, 21, 50\}$, $b_{MS} \in \{1, 4, 10, 13\}$.

these tasks. Both DOFA and SenPaMAE also tend to retain stable performance across the range, suggesting that the pre-training paradigms of any-sensor models likely contribute to this behavior.

4.4. Scale invariance

We evaluate scale invariance through k NN classification across two multispectral and one RGB dataset, as presented in Fig. 4 (below). The MS datasets include ⑧ EuroSAT [19] and ⑨ Brick Kiln [28], both modified according to GEO-Bench specifications [27]. For RGB assessment, we utilize the ⑪ RESISC45 [7] dataset since it exhibits a large variance in GSDs natively, which we further augment. The MS datasets feature fixed GSDs of 10 m. Following the protocol established by Reed et al. [43], we systematically downsample the test sets to progressively coarser GSDs to assess model robustness to spatial resolution degradation.

For the MS datasets, Panopticon’s representations remain very stable across the GSD range and perform better than the competition. For RESISC45, we find that all models have significantly lower performance at lower GSD ratios, likely due to the nature of detecting relatively small solar panels within spatially degraded images.

4.5. Benchmark performance on popular sensors

We compare existing many- and any-sensor models on the 6 classification and 6 segmentation datasets from GEO-Bench. We substitute ⑫ BigEarthNet-S2 and ⑬ BigEarthNet-S1 for m-bigearthnet available in GEO-bench, as it is upgraded with more robust splits and lower label noise [9]. These benchmark tasks represent a wide range of real-world downstream tasks on S1, S2, Landsat 8, RGB, and RGBN sensors. We include ⑪ RESISC45 [7] as an additional RGB land cover classification task, as well as an additional 9 tasks from ⑭–⑳ GEO-Bench [27]. An abridged summary of results is shown in Tab. 3. The complete GEO-Bench tables, along with the descriptions of the tasks, can be found in the supplementary materials.

Panopticon exhibits SOTA results on most tasks, and is competitive on the rest, showing that the model can also perform well on popular open source sensor datasets.

5. Ablation studies

We perform ablation studies on both pretraining stages following Section 3.5 configurations but reducing to 30 epochs with an effective batch size of 300. To evaluate cross-modality performance, we define four aggregated metrics: i) \mathbf{MS}_{acc} : average k NN accuracy on m-eurosat (with and without RGB channels), ii) $\mathbf{SAR}_{\text{acc}}$: average accuracy combining k NN and linear probing on eurosat-sar [59], iii) $\mathbf{Sim}_{\text{mAP}}$: average mAP across two Corine tasks and iv) \mathbf{Avg} : average across all individual tasks (see Tab. 8 in supplements). Our key findings show that larger dimensions in

channel attention relative to backbone, spectral progressive pretraining, and spectral positional embeddings are crucial for optimal performance.

Channel attention architecture We sweep different number of heads n_h and embedding dimensions D_{attn} in the cross attention in our patch embedding on stage 1 using two learning rates with 15 epochs each. Results can be seen in Tab. 5. Most notably, using $D_{\text{attn}} \geq 1536$ improves performance significantly compared to $D_{\text{attn}} = 768$. The influence of n_h is less profound.

Progressive pre-training We ablate the dataset composition of the first stage of our pre-training in Tab. 4. We can see that learning with multiple datasets, i.e. with more diverse sensors, leads to suboptimal results. This motivated a two-stage progressive pre-training approach. Among the single dataset runs, MMEarth seems best suited to learn SAR while SatlasPretrain learns generalization to other channels well. According to the Avg metric, fMoW performs best overall and is selected as dataset for the first stage of pre-training.

View selection During training, we sample a footprint and obtain two views from that location. One of the main assumptions of Panopticon, c.f. Sec. 3.1, is that having multiple views helps to distill knowledge between different sensors. In Tab. 4, we present an ablation (‘single’) that was trained using a single view during view generation — indeed, not utilizing multiple views does degrade performance.

Spectral embedding In Tab. 4, we compare our proposed embedding of encoding individual wavelengths and SAR configurations (‘fine-PE’) against a coarse embedding that only differentiates between SAR and optical embeddings (‘coarse’), no embedding at all (‘none’), and an embedding that additionally encodes the standard deviation of the SRF of optical sensors (‘fine-std’); see Sec. D for details. For optical sensors, having fine-grained spectral information substantially improves performance while adding information about the standard deviation does not seem to help. For SAR, a coarser embedding may be sufficient for these tasks. However, note that none of the downstream datasets include SAR data outside of a single transmit and receiver polarization (VV+VH). Assessing the efficacy of additional sensor metadata such as SRFs proved difficult to validate in practice due to the lack of sensor diversity in evaluation datasets.

			<i>Avg</i> \uparrow	<i>MS_{acc}</i> \uparrow	<i>SAR_{acc}</i> \uparrow	<i>Sim_{mAP}</i> \uparrow
Stage 1	Default	fMoW	83.5	92.2	75.8	79.6
	Datasets	MME	81.7	86.4	81.7	80.8
		SP	81.2	84.4	77.5	82.1
		fMoW, SP, MME	77.0	81.2	77.8	78.2
		fMoW, SP, MME, SE	73.9	79.1	74.4	76.8
Stage 2	Default	Fine PE, multi-view	86.8	93.1	82.2	83.4
	PE	None	84.8	91.5	81.2	80.7
		Coarse	85.1	91.0	82.1	80.8
		Fine-std	85.9	91.7	82.9	80.4
	Views	Single	82.2	84.2	78.8	83.0

Table 4. Ablations of major design decisions of Panopticon, according to pretraining stages. The metrics are averages in % over several tasks indicating general performance of specific sensors. SP = SatlasPretrain, SE = SpectralEarth, and MME = MMEarth.

$n_h \downarrow$	D_{attn}			
	768	1536	2304	3072
12	77.7	82.4	83.9	-
16	77.8	84.9	85.8	81.5
24	-	83.8	<u>85.5</u>	84.4
32	-	-	-	82.1

Table 5. Ablation of the channel attention architecture. MS_{acc} metric reported when changing the number of heads n_h in the rows and embedding dimension D_{attn} in the columns.

6. Discussion and conclusion

In this work, we introduced Panopticon, a flexible any-sensor foundation model that processes data from arbitrary sensor configurations without sensor-specific adaptations. By extending DINOv2 with multi-sensor view generation, spectral subsampling, and cross-attention over channels, our approach achieves state-of-the-art performance on standard benchmarks while demonstrating superior generalization to unique sensor configurations. We conducted rigorous evaluation on a battery of tests designed to evaluate the inherent sensor-agnostic capabilities of the model, from reducing spatial and spectral information, to evaluating cross-sensor generalization between training and test sets. Our findings demonstrate that Panopticon consistently outperforms existing state-of-the-art many-sensor and any-sensor models in developing truly sensor-agnostic representations. Tests on datasets outside typical training distributions (DigitalTyphoon, TropicalCyclone, and simulated MODIS and SuperDove configurations) revealed that most models can adapt to novel sensor modalities, though with varying degrees of success. Panopticon demonstrated particular strength in these cross-sensor scenarios. Notably, our

experiments also revealed that DINOv2, when combined with appropriate domain adaptation techniques, serves as a surprisingly strong baseline for RGB applications and certain MS use cases.

Our evaluation across 22 diverse tasks represents a significant step towards validating any-sensor capabilities, though important limitations remain. We did not explore temporal invariance or equivariance—a critical direction for future work. Furthermore, we could not fully explore promising directions such as incorporating channel bandwidth information and using spectral convolution as an augmentation strategy to generate arbitrary multispectral channels from hyperspectral data, which remain promising future directions.

While Panopticon explicitly models channel-level sensor characteristics, it relies on view augmentations to learn other important EO invariances related to capture time, processing levels, and ground sampling distance. Though we specifically tested and validated the latter, the other properties proved challenging to isolate and evaluate. Our results suggest that combining explicit spectral modeling with diverse augmentation strategies offers a promising path toward truly sensor-agnostic Earth observation.

The development of robust any-sensor models is hampered by the scarcity of machine learning-ready data from diverse satellite platforms—a limitation that constrains research progress and impedes equitable planetary monitoring [46]. As remote sensing platforms proliferate, frameworks like Panopticon that generalize across sensor configurations will become increasingly valuable for maximizing scientific and societal benefits. Future work should incorporate additional sensor-specific inductive biases, expand temporal modeling capabilities, and develop comprehensive cross-sensor evaluation benchmarks to advance this emerging field.

Acknowledgments

This material is based upon work supported by the National Science Foundation under Grant No. DGE- 2125913. The authors gratefully acknowledge the computing time provided on the high-performance computer HoreKa by the National High-Performance Computing Center at KIT (NHR@KIT). This center is jointly supported by the Federal Ministry of Education and Research and the Ministry of Science, Research and the Arts of Baden-Württemberg, as part of the National High-Performance Computing (NHR) joint funding program³. HoreKa is partly funded by the German Research Foundation (DFG). The authors are also grateful to Prof. Joshua Blumenstock, and the Berkeley High Performance Computing (Savio) department for the provisioning of computing infrastructure.

References

- [1] Guillaume Astruc, Nicolas Gonthier, Clement Mallet, and Loic Landrieu. AnySat: An Earth observation model for any resolutions, scales, and modalities. *arXiv preprint arXiv:2412.14123*, 2024. 1, 2
- [2] Yujia Bao, Srinivasan Sivanandan, and Theofanis Karaletsos. Channel vision transformers: An image is worth $c \times 16 \times 16$ words. *arXiv preprint arXiv:2309.16108*, 2023. 4
- [3] Favyen Bastani, Piper Wolters, Ritwik Gupta, Joe Ferdinando, and Aniruddha Kembhavi. Satlaspretrain: A large-scale dataset for remote sensing image understanding. In *Proceedings of the IEEE/CVF International Conference on Computer Vision*, pages 16772–16782, 2023. 4
- [4] Nassim Ait Ali Braham, Conrad M Albrecht, Julien Mairal, Jocelyn Chanussot, Yi Wang, and Xiao Xiang Zhu. Spectraearth: Training hyperspectral foundation models at scale. *arXiv preprint arXiv:2408.08447*, 2024. 2, 4, 6, 7, 5
- [5] Olivier Burggraaff. Biases from incorrect reflectance convolution. *Optics express*, 28(9):13801–13816, 2020. 2
- [6] Mathilde Caron, Hugo Touvron, Ishan Misra, Hervé Jégou, Julien Mairal, Piotr Bojanowski, and Armand Joulin. Emerging properties in self-supervised vision transformers. In *Proceedings of the IEEE/CVF International Conference on Computer Vision (ICCV)*, pages 9650–9660, 2021. 3
- [7] Gong Cheng, Junwei Han, and Xiaoqiang Lu. Remote sensing image scene classification: Benchmark and state of the art. *Proceedings of the IEEE*, 105(10):1865–1883, 2017. 8
- [8] Gordon Christie, Neil Fendley, James Wilson, and Ryan Mukherjee. Functional map of the world. In *Proceedings of the IEEE Conference on Computer Vision and Pattern Recognition*, pages 6172–6180, 2018. 4, 1
- [9] Kai Norman Clasen, Leonard Hackel, Tom Burgert, Gencer Sumbul, Begüm Demir, and Volker Markl. reben: Refined bigearthnet dataset for remote sensing image analysis. *arXiv preprint arXiv:2407.03653*, 2024. 6, 8
- [10] Shane R Cloude and Eric Pottier. A review of target decomposition theorems in radar polarimetry. *IEEE transactions on geoscience and remote sensing*, 34(2):498–518, 1996. 4
- [11] Yezhen Cong, Samar Khanna, Chenlin Meng, Patrick Liu, Erik Rozi, Yutong He, Marshall Burke, David B. Lobell, and Stefano Ermon. SatMAE: Pre-training transformers for temporal and multi-spectral satellite imagery. In *Advances in Neural Information Processing Systems*, 2022. 1, 2, 4
- [12] Michel Foucault. Panopticism. In *The information society reader*, pages 302–312. Routledge, 2020. 1
- [13] Anthony Fuller, Koreen Millard, and James Green. Croma: Remote sensing representations with contrastive radar-optical masked autoencoders. *Advances in Neural Information Processing Systems*, 36:5506–5538, 2023. 1, 2
- [14] Priya Goyal, Piotr Dollár, Ross Girshick, Pieter Noordhuis, Lukasz Wesolowski, Aapo Kyrola, Andrew Tulloch, Yangqing Jia, and Kaiming He. Accurate, large minibatch sgd: Training imagenet in 1 hour, 2018. 5
- [15] Luis Guanter, Hermann Kaufmann, Karl Segl, Saskia Forster, Christian Rogass, Sabine Chabrillat, Theres Kuester, André Hollstein, Godela Rossner, Christian Chlebek, et al. The enmap spaceborne imaging spectroscopy mission for earth observation. *Remote Sensing*, 7(7):8830–8857, 2015. 2
- [16] Boran Han, Shuai Zhang, Xingjian Shi, and Markus Reichstein. Bridging remote sensors with multisensor geospatial foundation models. In *Proceedings of the IEEE/CVF Conference on Computer Vision and Pattern Recognition*, pages 27852–27862, 2024. 2
- [17] Kaiming He, Xinlei Chen, Saining Xie, Yanghao Li, Piotr Dollár, and Ross Girshick. Masked autoencoders are scalable vision learners, 2021. 2
- [18] Patrick Helber, Benjamin Bischke, Andreas Dengel, and Damian Borth. Eurosat: A novel dataset and deep learning benchmark for land use and land cover classification. *IEEE Journal of Selected Topics in Applied Earth Observations and Remote Sensing*, 12(7):2217–2226, 2019. 7
- [19] Chia-Yu Hsu, Wenwen Li, and Sizhe Wang. Geospatial foundation models for image analysis: Evaluating and enhancing nasa-ibm prithvi’s domain adaptability. *International Journal of Geographical Information Science*, pages 1–30, 2024. 2, 6, 8
- [20] Jeremy Irvin, Lucas Tao, Joanne Zhou, Yuntao Ma, Langston Nashold, Benjamin Liu, and Andrew Y Ng. Usat: A unified self-supervised encoder for multi-sensor satellite imagery. *arXiv preprint arXiv:2312.02199*, 2023. 2
- [21] Johannes Jakubik, Sujit Roy, CE Phillips, Paolo Fraccaro, Denys Godwin, Bianca Zadrozny, Daniela Szwarcman, Carlos Gomes, Gabby Nyirjesy, Blair Edwards, et al. Foundation models for generalist geospatial artificial intelligence. *arXiv preprint arXiv:2310.18660*, 2023. 1
- [22] Johannes Jakubik, Sujit Roy, C. E. Phillips, Paolo Fraccaro, Denys Godwin, Bianca Zadrozny, Daniela Szwarcman, Carlos Gomes, Gabby Nyirjesy, Blair Edwards, Daiki Kimura, Naomi Simumba, Linsong Chu, S. Karthik Mukkavilli, Devyani Lambhate, Kamal Das, Ranjini Bangalore, Dario Oliveira, Michal Muszynski, Kumar Ankur, Muthukumar Ramasubramanian, Iksha Gurung, Sam Khallaghi, Hanxi, Li, Michael Cecil, Maryam Ahmadi, Fatemeh Kordi, Hamed Alemohammad, Manil Maskey, Raghu Ganti,

³<https://www.nhr-verein.de/en/our-partners>

- Kommy Weldemariam, and Rahul Ramachandran. Foundation Models for Generalist Geospatial Artificial Intelligence, 2023. arXiv:2310.18660 [cs]. 2
- [23] Hannah Kerner, Snehal Chaudhari, Aninda Ghosh, Caleb Robinson, Adeel Ahmad, Eddie Choi, Nathan Jacobs, Chris Holmes, Matthias Mohr, Rahul Dodhia, et al. Fields of the World: A machine learning benchmark dataset for global agricultural field boundary segmentation. *arXiv preprint arXiv:2409.16252*, 2024. 1
- [24] Ethan King, Jaime Rodriguez, Diego Llanes, Timothy Doster, Tegan Emerson, and James Koch. Stars: Sensor-agnostic transformer architecture for remote sensing. *arXiv preprint arXiv:2411.05714*, 2024. 4
- [25] Asanobu Kitamoto, Jared Hwang, Bastien Vuillod, Lucas Gautier, Yingtao Tian, and Tarin Clanuwat. Digital typhoon: Long-term satellite image dataset for the spatio-temporal modeling of tropical cyclones. *Advances in Neural Information Processing Systems*, 36:40623–40636, 2023. 6
- [26] Ridvan Salih Kuzu, Frauke Albrecht, Caroline Arnold, Roshni Kamath, and Kai Konen. Predicting soil properties from hyperspectral satellite images. In *2022 IEEE International Conference on Image Processing (ICIP)*, pages 4296–4300, 2022. 6
- [27] Alexandre Lacoste, Nils Lehmann, Pau Rodriguez, Evan Sherwin, Hannah Kerner, Björn Lütjens, Jeremy Irvin, David Dao, Hamed Alemohammad, Alexandre Drouin, et al. Geobench: Toward foundation models for earth monitoring. *Advances in Neural Information Processing Systems*, 36, 2024. 2, 6, 7, 8
- [28] Jihyeon Lee, Nina R Brooks, Fahim Tajwar, Marshall Burke, Stefano Ermon, David B Lobell, Debashish Biswas, and Stephen P Luby. Scalable deep learning to identify brick kilns and aid regulatory capacity. *Proceedings of the National Academy of Sciences*, 118(17):e2018863118, 2021. 7, 8
- [29] Xuyang Li, Danfeng Hong, and Jocelyn Chanussot. S2MAE: A spatial-spectral pretraining foundation model for spectral remote sensing data. In *Proceedings of the IEEE/CVF Conference on Computer Vision and Pattern Recognition*, pages 24088–24097, 2024. 1, 2
- [30] Lei Ma, Yu Liu, Xueliang Zhang, Yuanxin Ye, Gaofei Yin, and Brian Alan Johnson. Deep learning in remote sensing applications: A meta-analysis and review. *ISPRS journal of photogrammetry and remote sensing*, 152:166–177, 2019. 1
- [31] Sahel Mahdavi, Meisam Amani, and Yasser Maghsoudi. The effects of orbit type on synthetic aperture radar (sar) backscatter. *Remote sensing letters*, 10(2):120–128, 2019. 4
- [32] Utkarsh Mall, Bharath Hariharan, and Kavita Bala. Change-Aware Sampling and Contrastive Learning for Satellite Images. In *2023 IEEE/CVF Conference on Computer Vision and Pattern Recognition (CVPR)*, pages 5261–5270, Vancouver, BC, Canada, 2023. IEEE. 3
- [33] Manil Maskey, Rahul Ramachandran, Iksha Gurung, Brian Freitag, Muthukumaran Ramasubramanian, and Jeffrey Miller. Tropical cyclone wind estimation competition dataset. *Version 1.0, Radiant MLHub*, 2022. 6
- [34] Oscar Mañas, Alexandre Lacoste, Xavier Giro-i Nieto, David Vazquez, and Pau Rodriguez. Seasonal Contrast: Unsupervised Pre-Training from Uncurated Remote Sensing Data, 2021. arXiv:2103.16607 [cs]. 3
- [35] Matías Mendieta, Boran Han, Xingjian Shi, Yi Zhu, and Chen Chen. Towards geospatial foundation models via continual pretraining. In *Proceedings of the IEEE/CVF International Conference on Computer Vision*, pages 16806–16816, 2023. 4
- [36] Vishal Nedungadi, Ankit Karirayaa, Stefan Oehmcke, Serge Belongie, Christian Igel, and Nico Lang. Mmearth: Exploring multi-modal pretext tasks for geospatial representation learning. *arXiv preprint arXiv:2405.02771*, 2024. 4, 2
- [37] Tung Nguyen, Johannes Brandstetter, Ashish Kapoor, Jayesh K Gupta, and Aditya Grover. Climax: A foundation model for weather and climate. *arXiv preprint arXiv:2301.10343*, 2023. 4
- [38] Mubashir Noman, Muzammal Naseer, Hisham Cholakkal, Rao Muhammad Anwer, Salman Khan, and Fahad Shahbaz Khan. Rethinking transformers pre-training for multi-spectral satellite imagery. In *Proceedings of the IEEE/CVF Conference on Computer Vision and Pattern Recognition*, pages 27811–27819, 2024. 1
- [39] Maxime Oquab, Timothée Darcet, Théo Moutakanni, Huy Vo, Marc Szafraniec, Vasil Khalidov, Pierre Fernandez, Daniel Haziza, Francisco Massa, Alaaeldin El-Nouby, et al. Dinov2: Learning robust visual features without supervision. *arXiv preprint arXiv:2304.07193*, 2023. 1, 3
- [40] Fernando Paolo, Tsu-ting Tim Lin, Ritwik Gupta, Bryce Goodman, Nirav Patel, Daniel Kuster, David Kroodsma, and Jared Dunmon. xView3-SAR: Detecting dark fishing activity using synthetic aperture radar imagery. *Advances in Neural Information Processing Systems*, 35:37604–37616, 2022. 1
- [41] Jonathan Prexl and Michael Schmitt. Multi-Modal Multi-Objective Contrastive Learning for Sentinel-1/2 Imagery. In *2023 IEEE/CVF Conference on Computer Vision and Pattern Recognition Workshops (CVPRW)*, Vancouver, BC, Canada, 2023. IEEE. 2
- [42] Jonathan Prexl and Michael Schmitt. Senpa-mae: Sensor parameter aware masked autoencoder for multi-satellite self-supervised pretraining. *arXiv preprint arXiv:2408.11000*, 2024. 1, 2
- [43] Colorado J Reed, Ritwik Gupta, Shufan Li, Sarah Brockman, Christopher Funk, Brian Clipp, Kurt Keutzer, Salvatore Candido, Matt Uyttendaele, and Trevor Darrell. Scale-mae: A scale-aware masked autoencoder for multiscale geospatial representation learning. In *Proceedings of the IEEE/CVF International Conference on Computer Vision*, pages 4088–4099, 2023. 1, 7, 8, 5
- [44] Felix Rembold, Clement Atzberger, Igor Savin, and Oscar Rojas. Using low resolution satellite imagery for yield prediction and yield anomaly detection. *Remote Sensing*, 5(4): 1704–1733, 2013. 1
- [45] Esther Rolf, Konstantin Klemmer, Caleb Robinson, and Hannah Kerner. Mission critical–satellite data is a distinct modality in machine learning. *arXiv preprint arXiv:2402.01444*, 2024. 1

- [46] Philippe Rufin, Patrick Meyfroidt, Felicia O Akinyemi, Lyndon Estes, Esther Shupel Ibrahim, Meha Jain, Hannah Kerner, Sá Nogueira Lisboa, David Lobell, Catherine Nakalembe, et al. To enhance sustainable development goal research, open up commercial satellite image archives. *Proceedings of the National Academy of Sciences*, 122(7): e2410246122, 2025. 6, 9
- [47] Adam Stewart, Nils Lehmann, Isaac Corley, Yi Wang, Yi-Chia Chang, Nassim Ait Ali Braham, Shradha Sehgal, Caleb Robinson, and Arindam Banerjee. SSL4EO-L: Datasets and foundation models for Landsat imagery. *Advances in Neural Information Processing Systems*, 36:59787–59807, 2023. 1
- [48] Adam J Stewart, Caleb Robinson, Isaac A Corley, Anthony Ortiz, Juan M Lavista Ferres, and Arindam Banerjee. TorchGeo: deep learning with geospatial data. In *Proceedings of the 30th international conference on advances in geographic information systems*, pages 1–12, 2022. 4, 2
- [49] Merugu Suresh and Kamal Jain. Change detection and estimation of illegal mining using satellite images. In *Proceedings of 2nd International conference of Innovation in Electronics and communication Engineering (ICIECE-2013)*, 2013. 1
- [50] Gabriel Tseng, Ruben Cartuyvels, Ivan Zvonkov, Mirali Purohit, David Rolnick, and Hannah Kerner. Lightweight, pre-trained transformers for remote sensing timeseries. *arXiv preprint arXiv:2304.14065*, 2023. 1
- [51] Gabriel Tseng, Anthony Fuller, Marlena Reil, Henry Herzog, Patrick Beukema, Favyen Bastani, James R Green, Evan Shelhamer, Hannah Kerner, and David Rolnick. Galileo: Learning global and local features in pretrained remote sensing models. *arXiv preprint arXiv:2502.09356*, 2025. 2
- [52] Arsenios Tsokas, Maciej Rysz, Panos M Pardalos, and Kathleen Dipple. Sar data applications in earth observation: An overview. *Expert Systems with Applications*, 205:117342, 2022. 1
- [53] Fawwaz T Ulaby, Daniel Held, Myron C Donson, Kyle C McDonald, and Thomas BA Senior. Relating polarization phase difference of sar signals to scene properties. *IEEE Transactions on Geoscience and Remote Sensing*, GE-25(1): 83–92, 1987. 4
- [54] Susan L Ustin and Elizabeth M Middleton. Current and near-term advances in earth observation for ecological applications. *Ecological Processes*, 10(1):1, 2021. 1, 4
- [55] Adam Van Etten, Dave Lindenbaum, and Todd M Bacastow. Spacenet: A remote sensing dataset and challenge series. *arXiv preprint arXiv:1807.01232*, 2018. 6
- [56] Ashish Vaswani, Noam Shazeer, Niki Parmar, Jakob Uszkoreit, Llion Jones, Aidan N Gomez, Łukasz Kaiser, and Illia Polosukhin. Attention is all you need. *Advances in neural information processing systems*, 30, 2017. 4
- [57] Yi Wang, Conrad M. Albrecht, and Xiao Xiang Zhu. Self-supervised Vision Transformers for Joint SAR-optical Representation Learning, 2022. arXiv:2204.05381 [cs]. 3
- [58] Yi Wang, Nassim Ait Ali Braham, Zhitong Xiong, Chenying Liu, Conrad M Albrecht, and Xiao Xiang Zhu. SSL4EO-S12: A large-scale multimodal, multitemporal dataset for self-supervised learning in Earth observation. *IEEE Geoscience and Remote Sensing Magazine*, 11(3):98–106, 2023. 1
- [59] Yi Wang, Hugo Hernández Hernández, Conrad M Albrecht, and Xiao Xiang Zhu. Feature guided masked autoencoder for self-supervised learning in remote sensing. *arXiv preprint arXiv:2310.18653*, 2023. 8, 6
- [60] Yi Wang, Conrad M. Albrecht, Nassim Ait Ali Braham, Chenying Liu, Zhitong Xiong, and Xiao Xiang Zhu. Decoupling Common and Unique Representations for Multimodal Self-supervised Learning, 2024. arXiv:2309.05300 [cs]. 2
- [61] Yi Wang, Conrad M Albrecht, and Xiao Xiang Zhu. Multi-label guided soft contrastive learning for efficient earth observation pretraining. *arXiv preprint arXiv:2405.20462*, 2024. 1
- [62] Xinye Wanyan, Sachith Seneviratne, Shuchang Shen, and Michael Kirley. Dino-mc: Self-supervised contrastive learning for remote sensing imagery with multi-sized local crops. *arXiv preprint arXiv:2303.06670*, 2023. 1
- [63] Xinye Wanyan, Sachith Seneviratne, Shuchang Shen, and Michael Kirley. Extending global-local view alignment for self-supervised learning with remote sensing imagery, 2024. arXiv:2303.06670 [cs]. 3
- [64] Zhitong Xiong, Yi Wang, Fahong Zhang, Adam J Stewart, Joëlle Hanna, Damian Borth, Ioannis Papoutsis, Bertrand Le Saux, Gustau Camps-Valls, and Xiao Xiang Zhu. Neural plasticity-inspired foundation model for observing the earth crossing modalities. *arXiv preprint arXiv:2403.15356*, 2024. 1, 2, 4
- [65] Zhitong Xiong, Yi Wang, Fahong Zhang, and Xiao Xiang Zhu. One for all: Toward unified foundation models for Earth vision. In *IGARSS 2024-2024 IEEE International Geoscience and Remote Sensing Symposium*, pages 2734–2738. IEEE, 2024. 1
- [66] Lixian Zhang, Yi Zhao, Runmin Dong, Jinxiao Zhang, Shuai Yuan, Shilei Cao, Mengxuan Chen, Juepeng Zheng, Weijia Li, Wei Liu, Wayne Zhang, Litong Feng, and Haohuan Fu. A²-MAE: A spatial-temporal-spectral unified remote sensing pre-training method based on anchor-aware masked autoencoder, 2024. arXiv:2406.08079 [cs] version: 2. 3
- [67] Jinghao Zhou, Chen Wei, Huiyu Wang, Wei Shen, Cihang Xie, Alan Yuille, and Tao Kong. iBOT: Image BERT Pre-Training with Online Tokenizer, 2022. arXiv:2111.07832 [cs]. 3

Panopticon: Advancing Any-Sensor Foundation Models for Earth Observation

Supplementary Material

A. Why Panopticon?

The idea of the *panopticon* was first suggested by the philosopher Jeremy Bentham as an ideal model for efficient prison design, where a single person could watch over an entire prison. Michel Foucault later reinterpreted it as a powerful metaphor for repressive systems of power, control and surveillance in modern societies [12], something that is perhaps even more relevant today with the proliferation of digital surveillance technologies.

We are well aware of the term’s loaded history and controversial connotations; so why choose it? We want to co-opt this term and flip its meaning, using it as a metaphor for systems that can keep a watchful and benevolent eye over our planet. Instead of surveilling people, Panopticon(s) can observe Earth itself—its changing landscapes, ecosystems, and climate patterns.

The beauty of our model is that, like the original panopticon concept, it provides comprehensive visibility from a single vantage point. But unlike Bentham’s prison design, our goal is not control and fear, but rather understanding and monitoring. There is also a technical parallel that we find fitting: the original panopticon was designed to see everything from a central position, regardless of where attention was directed. Similarly, our model can “look” through any sensor configuration without needing specific adaptations—a sensor-agnostic vision that mirrors the all-seeing nature of the conceptual panopticon, but repurposed for planetary good.

B. Code and data availability

All data loaders and model code will be contributed to the TorchGeo library for reproducibility and ease of future experimentation. GitHub links to the pre-training and evaluation codebases will be added after the end of the double-blind review period. All code is distributed under an MIT license, while all model weights are distributed under a CC-BY-4.0 license.

C. Datasets

C.1. Pre-training datasets

We organize the four pretraining datasets as shown in Tab. 1 by geographical footprint, where a footprint is defined by images having an exact geo-reference match. During pre-training, from each footprint, we randomly sample a number of “snapshots” as shown in Fig. 5.

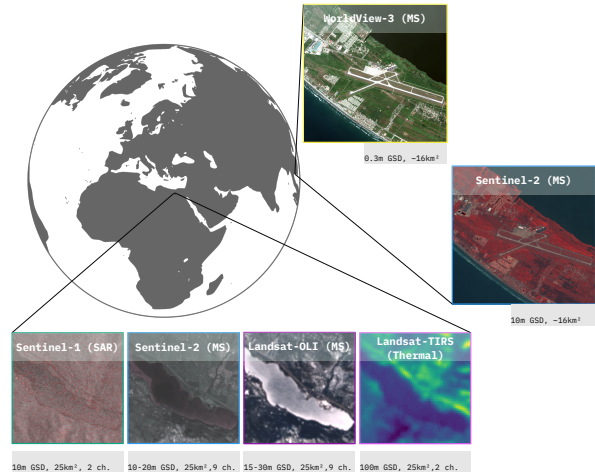


Figure 5. Snapshots: examples of snapshots taken from distinct footprints. Our pretraining dataset consists of various sensor modalities, channels, GSDs, scales, and timesteps acquired from across the Earth’s surface. Different channels, GSDs, and footprint sizes provide information about different attributes of the geospatial objects. Note: some images are shown in false colors to enable mapping from non-visible spectra.

fMoW fMoW [8] consists of data from 4 MS satellite sensors, QuickBird-1 and GeoEye-2 having 4 channels (RGB, NIR), while WorldView-2 and -3 have 8 channels, with GSDs typically ranging from 1–2 m. Additionally, the dataset also includes pansharpened versions of these same images in RGB which have a GSD < 1 m. This dataset was chosen for its global spatial coverage, wide spectral coverage⁴ and very low GSD values, along with extensive functional coverage of human modified land cover types. Moreover, this dataset also represents a large variance in time of capture, off-nadir angles, both of which affects illumination of targets. Since spatial footprints were available for all images, we generate an geographically indexed version of this dataset, which will be released with the rest of the code. Additionally, we remove images greater than 1024 px, which are typically the pansharpened RGB images, to reduce memory overheads.

fMoW-Sentinel fMoW-Sentinel [11] was created to be an exact copy of the locations captured by fMoW, but with Sentinel-2 imagery. We created a combined dataset

⁴including “non-standard” bands, i.e. those with spectral coverage outside those of the popular open-data sources such as Landsat and Sentinel series.

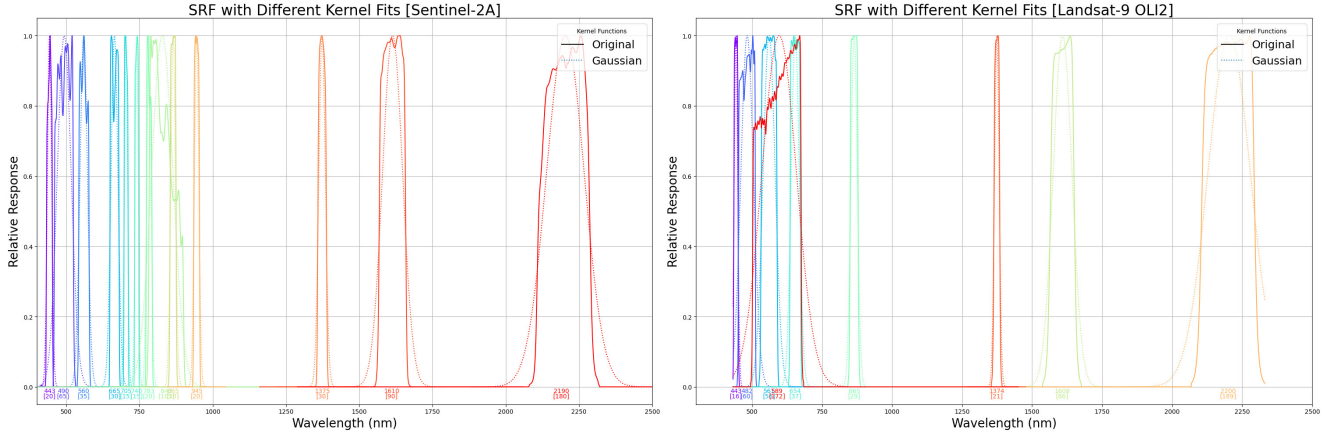


Figure 6. Spectral response function (SRF) fitting for Sentinel-2 (left) and Landsat 9 (right).

from fMoW and fMoW-Sentinel by indexing by footprint and sensor type. Together, these two datasets capture surface properties from five separate sensor platforms between 2002 and 2022, providing a lot of natural variation for a given footprint. Finally, the footprints of each image vary tremendously, from 0.2 to 25 km², providing a large range of features at different scales. This combined dataset consists of 89,666 unique footprints, where each footprint can have dozens of images across these sensors.

MMEarth MultiModal Earth (MMEarth) [36] was released as a paired dataset of multiple modalities that include Sentinel-1 SAR, Sentinel-2 MS, elevation, and other paired modalities. Most importantly, the Sentinel-2 data included multiple processing levels (L1C and L2A), and Sentinel-1 data was captured in all 4 polarization combinations (VV, VH, HH, HV) and in both orbits (ascending, descending). This data was primarily included to model the effects of polarization and orbit for SAR data and processing levels for optical. Moreover, this extensive dataset comprises of 1,239,937 unique footprints equitably distributed according to land cover types, each of which providing a pair of S-1 and S-2 images.

SpectralEarth SpectralEarth [4] is the largest open source hyperspectral dataset available at the time of writing comprising of 450K patches sampled globally by the EnMAP satellite [15], made available by the German Aerospace Center (DLR). This dataset additionally provides four downstream benchmark tasks using data from the same sensor, but utilizing non-overlapping patches, separate from pretraining. This dataset was included for its rich spectral diversity, enabling the model to learn HS characteristics and simulate any arbitrary multispectral band. SpectralEarth provides 538,927 unique footprints, each of which provides a single HS image of 202 bands.

SatlasPretrain SatlasPretrain consists of 30 TB of imagery across Sentinel-1, Sentinel-2, Landsat-9, and NAIP sensors. We utilize only the first three, as NAIP geographic coverage is limited to the United States and spectrally consists of only RGB and NIR bands. We created a unified indexed dataset comprising of 768,800 unique footprints, where each footprint can contain up to 3 sensor images taken across 2022. It is also the only large pretraining dataset to contain thermal images from the Landsat 9-TIRS sensor.

C.2. Evaluation datasets

We utilize the following benchmark task and datasets. Where possible, we utilized existing Python libraries such as TorchGeo [48] and GEO-Bench [27]. For a complete list of datasets, please consult Tab. 6.

The following section outlines any modifications we make to standard datasets:

SpaceNet We utilize the SpaceNet 1 dataset from TorchGeo, which is a building footprint segmentation task over the city of Rio de Janeiro with 8 band MS images and 3 band pansharpened RGB images captured by WorldView 2. We utilize only the 8-band images. Since the original dataset is only available with labels for the training set, we randomly split the dataset into training, validation and test splits with a 80:10:10 ratio.

D. Utilizing complete spectral information

In the field of *any-sensor* models, DOFA[64] utilizes the mean wavelength of channels within a hypernetwork to learn spectral encodings per channel, while SenPaMAE [42] utilizes the SRF to do the same. We experimented with the following mechanisms to incorporate SRF and/or bandwidth information per channel, in addition to the mean wavelength.

Index	Name	Name used in this paper	Modifications
①	Corine [SuperDove]		Spectral convolution from EnMap to Planet Superdove
②	Corine [MODIS]		Spectral convolution from EnMap to MODIS
③	Hyperview [SuperDove]		Spectral convolution from Intuition to SuperDove
④	Hyperview [MODIS]		Spectral convolution from Intuition to MODIS
⑤	TropicalCyclone	TC	TorchGeo, we use 10% of train
⑥	DigitalTyphoon	DT	TorchGeo, we use 10% of train
⑦	SpaceNet 1	SpaceNet 1	Randomly split the train set into train, val, and test (80:10:10)
⑧	EuroSAT	m-eurosat	GEO-Bench
⑨	BrickKiln	m-brick-kiln	GEO-Bench
⑩	EnMAP-Corine	Corine	Original 202 band dataset
⑪	RESISC45	RESISC	GEO-Bench
⑫	BENV2-S2		
⑬	BENV2-S1		
⑭	ForestNet	m-forestnet	GEO-Bench
⑮	So2Sat	m-so2sat	GEO-Bench
⑯	PV4Ger (cls.)	m-pv4ger	GEO-Bench
⑰	PV4Ger (segm.)	m-pv4ger-seg	GEO-Bench
⑱	Chesapeake Landcover	m-chesapeake-landcover	GEO-Bench
⑲	Cashew Plantation	m-cashew-plantation	GEO-Bench
⑳	SA Crop Type	m-SA-crop-type	GEO-Bench
㉑	NZ Cattle	m-nz-cattle	GEO-Bench
㉒	NEON Tree	m-NeonTree	GEO-Bench

Table 6. Summary of all evaluation datasets and the modifications made to them.

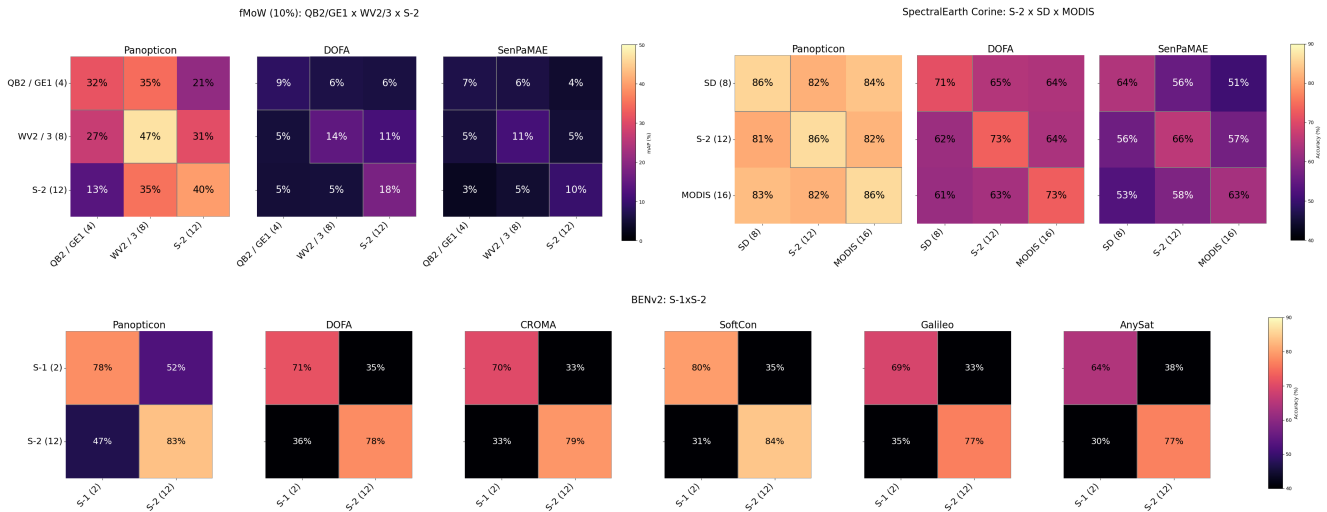


Figure 7. Cross-sensor invariance (absolute values). In addition to train/val/test splits, we also split datasets across sensors to explicitly test sensor invariance. y -axes on the heatmap represent training sensors and x -axes, test sensors. The diagonals represent same-sensor for train and test, while off-diagonal elements represent cross-sensor results with all values expressed as absolute performance values as percentages. **Left:** splits are across QuickBird-2 (QB2) / GeoEye-1 (GE1) which are RGB-NIR. **Right:** splits are across synthesized sensors from the HS EnMAP sensor using spectral convolution - MODIS, Sentinel-2 and Planet SuperDove, for any-sensor models. **Bottom:** BigEarthNet-v2; splits are implemented across Sentinel-1 and Sentinel-2 sensors, for all any-sensor and many-sensor models, except SenPaMAE which cannot process SAR imagery. Panopticon consistently outperforms other models in both settings. Note that the value ranges differ for each sub-figure.

Spectral integrated positional encoding To achieve sensor agnosticism, we introduce a novel spectral integrated positional encoding (sIPE) that leverages known sensor characteristics. Building on the channel-wise attention mechanism from Nguyen et al. [37], we model each sensor’s SRF as an un-normalized Gaussian kernel characterized by its mean, μ and standard deviation, σ . This was inspired by noticing that such a Gaussian kernel provides a relatively good fit for SRFs, such as Sentinel-2A and Landsat-9 OLI sensors as shown in Fig. 6. We also experimented with Epanechnikov kernel fitting, which provided better R^2 results, but since Gaussians are well understood and have closed-form solutions - they tend to be easier to work with. This allows us to summarize and model a SRF with a set of $\{\mu, \sigma\}$ pairs.

We then extend absolute positional embeddings [56] to incorporate this spectral information through integration against sinusoidal basis functions:

$$\begin{aligned} \text{PE}_{\text{spectral}}(\mu, \sigma, 2i) &= \int e^{-\frac{(\mu-\lambda)^2}{2\sigma^2}} \cdot \sin(\omega_i \lambda) \cdot d\lambda, \\ \text{PE}_{\text{spectral}}(\mu, \sigma, 2i+1) &= \int e^{-\frac{(\mu-\lambda)^2}{2\sigma^2}} \cdot \cos(\omega_i \lambda) \cdot d\lambda, \end{aligned} \quad (3)$$

where ω is a hyper-parameter typically set to $\frac{1}{10000^{\frac{2i}{D}}}$ and $i \in (0, D]$.

We derive the closed-form solution for Eq. (3) as follows:

$$\begin{aligned} \text{PE}_{\text{spectral}}(\mu, \sigma, 2i) &= \sigma\sqrt{2\pi} \cdot e^{-\frac{\omega_i^2 \sigma^2}{2}} \cdot \sin(\omega_i \mu), \\ \text{PE}_{\text{spectral}}(\mu, \sigma, 2i) &= \sigma\sqrt{2\pi} \cdot e^{-\frac{\omega_i^2 \sigma^2}{2}} \cdot \cos(\omega_i \mu). \end{aligned} \quad (4)$$

Eq. (4) allows us to quickly generate spectral PEs that are added to channel tokens. Our hypothesis was that while the query learns how best to fuse spectral tokens across channels, it can only do so based on the extracted low-level features within those patches. Adding the sIPE to the patch tokens provides a spectral inductive bias to each token relative to its central wavelength and bandwidth, effectively grounding the patch token to its physical capture attributes.

Spectral convolution Inspired by King et al. [24], we employ spectral convolution as a spectral augmentation for HS inputs. Given a source HS image comprised of i channels, $x^s(\lambda)$, and its spectral response function (SRF), $\text{SRF}_s(\lambda)$, a spectral convolution, R is defined as the integral of the product of $x^s(\lambda)$ and $\text{SRF}_s(\lambda)$, normalized by the integral of its SRF. We additionally correct this to account for the SRF of the target, $\text{SRF}_t(\lambda)$:

$$R = \frac{\sum_{i=1}^{N_s} \int_{\lambda_{\min}}^{\lambda_{\max}} x_i^s(\lambda) \text{SRF}_t(\lambda) \text{SRF}_s(\lambda) d\lambda}{\int_{\lambda_{\min}}^{\lambda_{\max}} \text{SRF}_t(\lambda) \text{SRF}_s(\lambda) d\lambda} \quad (5)$$

Table 7. Performance metrics for Panopticon-IPE across various datasets

Dataset	Score
<i>Classification (Accuracy %)</i>	
m-eurosat	96.1
m-brick-kiln	95.8
m-pv4ger-cls	95.8
RESISC45	91.2
m-forestnet	54.0
<i>Segmentation (mIoU %)</i>	
m-pv4ger	95.4
m-nzcattle	92.8
spacenet1	90.3
m-neontree	79.6
m-chesapeake	78.0
m-cashew	59.1
m-sacrop	52.3
<i>Multi-Label Classification (mAP %)</i>	
Corine-MODIS	80.0
Corine-SuperDove	79.8
<i>Regression (MSE)</i>	
DigitalTyphoon	0.93
Hyperview-MODIS	0.35
Hyperview-SuperDove	0.35
TropicalCyclone	0.28

To generate arbitrary MS channels with unknown SRFs, we model their SRF, SRF_t as un-normalized Gaussian kernel with a mean wavelength, λ_t , and standard deviation, σ_t . We apply Equation 5 c times to generate a single MS image comprised of c bands, with defined spectral characteristics. Through this process, we are able to generate novel multi-spectral views from any HS source, extensively expanding the spectral augmentation capabilities of this framework. We hypothesize that this combination may prove to add useful spectral inductive biases to the model.

Evaluation To evaluate these design choices, we run the evaluation suite on a model trained according to the specifications laid out in Sec. 3.5, i.e. identical to the model described in the main paper. We call this model Panopticon-IPE. The results are shown in Tab. 7.

Comparing these results to Tab. 2, Tab. 9, and Tab. 10, we see that Panopticon-IPE is relatively close in performance to Panopticon, and in some cases (TropicalCyclone) even excels. However, on average this model performs worse than our default settings, and as a result, we did not include these methods in the main paper. We leave these findings for the benefit of future researchers.

E. Technical details

E.1. Pre-training

Hyperparameters We follow most of the DINOv2 configuration with the following significant changes:

- We multiply the learning rate of the backbone by 0.2, de-prioritizing learning the backbone.
- We reduce the iBOT loss weight to 0.1 based on early ablation studies.
- We removed the Kolo loss.

We performed early off-the-record ablations on these. Apart from that, and for both stages 1 and 2, we train for 70 artificial epochs with 1250 iterations each, with the AdamW optimizer, a base learning rate of $5e-4$, standard learning rate scaling $lr \cdot bsz/256$, a linear warmup for 5 epochs followed by a cosine decay to a minimum $1e-6$ learning rate.

Metrics For details on the metrics, see Tab. 8.

Spectral subsampling When evaluating model choices during pretraining, we subsample the SpectralEarth Corine classification dataset [4] to include only 21 bands. The 202 available bands were first binned into 21 contiguous groups and then a single HS channel was randomly sampled from each bin to generate a spectrally representative sample. The datasets above were chosen to represent RGB, MS, HS, and SAR data over a range of GSDs to test the generalization capabilities of each model.

E.2. Evaluation

All tasks were executed on either 40 GB A100 or 48 GB L40S GPU. The batch size is optimized for each task and model to maximize GPU memory and the base learning rate lr is scaled by the batch size according to the linear scaling rule $lr \cdot \text{batch size}/256$ [14]. In our evaluations, we use 4 different task types.

k NN k -nearest neighbors (k NN) between train and test sets evaluates representation quality by measuring how accurately a test sample’s label can be predicted from its k nearest training samples in the embedding space. For Fig. 4, we keep $k = 20$ following Reed et al. [43].

Linear probing We mainly follow the implementation of DINOv2 and sweep multiple extraction methods. In particular, we extract the tokens from the last one or four transformer blocks and aggregate them by concatenating the cls tokens, average pooling, or the default aggregation suggested by the specific model at hand. For each aggregation, we sweep the base learning rates: [$1e-5$, $5e-5$, $1e-4$, $5e-4$, $1e-3$, $5e-3$, $1e-2$, $5e-2$, 0.1, 0.5, 1, 5, 10], resulting in $2 \cdot 3 \cdot 13 = 78$ runs. Note that we use an extension

of the DINOv2 implementation that computes all these different configurations simultaneously from a single forward pass of the backbone. This amortizes the time needed for computing the forward pass, significantly reducing overall training time. We train for 50 epochs with a 0.9 momentum Stochastic Gradient Descent optimizer. We also add a trainable batch normalization before the linear head. For the cross-sensor evaluations in Fig. 3 and Fig. 7, we only extract tokens from the last transformer block to ease compatibility issues across models that use different encoders for SAR and optical modalities.

Linear probing with re-initialized patch embedding

We replace the patch embedding of the model with a randomly initialized 2D convolution layer with the correct number of channels of the dataset at hand. We add a trainable batch norm and linear head to the encoder, unfreeze the new patch embedding and freeze the remaining encoder. Since the patch embedding is trainable, the forward passes of backbones are different between each configuration and cannot be amortized as in linear probing anymore. Therefore, we fix the feature aggregation to the default one suggested by the model authors and sweep the base learning rates: [0.01, 0.001, 0.0005, 0.0001] with 50 epochs each, stochastic gradient descent optimizer and 5 epochs of learning rate warmup.

AnySat and Galileo presented unique challenges due to the way they implement modality specific encoders. For AnySat, we pick a specific modality, and retrain the 2D convolution layer of that branch; we picked the NAIP encoder since it does not implement temporal attention, which consumes significant memory and compute. For Galileo, this was not possible since they use a channel grouping where each group produces a set of independent tokens, unlike other models where the channel dimension is collapsed. To replace this, we would have to create a new group with a custom number of channels which would break how Galileo processes tokens in groups. Furthermore, Galileo employs FlexiPatchEmbed, which is trained by randomizing the patch size during pretraining. To properly train this module, we would need to mimic that during evaluation, which was beyond the scope of the evaluation phase of this paper. Therefore, we omitted evaluating Galileo in tests that required retraining the patch embed module for domain adaptation.

Semantic segmentation We freeze the backbone and add trainable standard modules from the mmsegmentation library. In particular, we use a Feature2Pyramid as neck, a UPerNet decoder and an auxiliary FCNHead. We sweep the base learning rates: [$1e-1$, $1e-2$, $1e-3$, $1e-4$, $1e-5$, $1e-6$] and utilize the AdamW optimizer for 50 epochs with no learning rate warmup.

Agg.	id	dataset	task details	metric
MS _{acc}	1	m-eurosat	k NN, $k = 20, T = 0.07$	top-1 overall accuracy
	2	m-eurosat without RGB channels	k NN, $k = 20, T = 0.07$	top-1 overall accuracy
SAR _{acc}	3	m-eurosat-SAR [59]	k NN, $k = 20, T = 0.07$	top-1 overall accuracy
	4	m-eurosat-SAR	linear probing for 10 epochs	top-1 overall accuracy
Sim _{mAP}	5	Corine-4	linear probing on 10% subset for 10 epochs	top-1 overall multilabel average precision
	6	Corine-12	linear probing on 10% subset for 10 epochs	top-1 overall multilabel average precision
Avg	1-6			
	7	RESISC45	k NN, $k = 20, T = 0.07$	top-1 overall accuracy
	8	m-eurosat only RGB channels	k NN, $k = 20, T = 0.07$	top-1 overall accuracy

Table 8. Metrics used to inform design decisions and reported in Ablation section of the main text. The aggregation metric is computed as the average of all its metrics. Corine- n denotes the Corine dataset subsampled to n randomly-selected channels.

Model adaptations During evaluation, we picked the image size that the model was natively trained on to maximize that model’s ability to produce representations.

F. Additional ablations

Spectral augmentation In line with the DINO ablation on scales in random resized crops, we ablate our spectral size as $(1, s), (s, 13)$ for $s \in \{2, 4, 8, 13\}$. Similarly to DINO, $s = 4$ constituting roughly 1/3 of the full information performs best as can be seen in Tab. 11

	m-brick-kiln (S2)	m-eurosat (S2)	m-forestnet (L8)	m-pv4ger (RGB)	m-so2sat (S2)	BENv2 (S2)
DINOv2	97.5	95.5	53.5	97.5	60.8	80.1
CROMA	94.5	91.1	-	-	53.5	79.4
SoftCon	94.9	92.2	-	-	52.1	80.6
AnySat	tbd	87.6	50.9	92.8	42.5	76.8
Galileo	93.1	88.6	-	-	54.2	76.5
SenPaMAE	83.9	77.5	33.5	87.1	33.7	63.8
DOFA	95.8	92.9	53.2	97.4	54.2	78.8
Panopticon	96.7	96.4	56.3	96.4	61.7	83.9

Table 9. GEO-Bench classification performance with BENv2, linear probing, overall accuracy, overall multi-label average precision for BENv2. All values are percentages.

	m-cashew (S2)	m-chesapeake (RGBN)	m-neontree (RGB)	m-nzcattle (RGB)	m-pv4ger (RGB)	m-sacrop (S2)
DINOv2	65.9	<u>78.5</u>	80.9	92.7	96.9	51.2
CROMA	44.3	-	-	-	-	48.4
SoftCon	54.5	-	-	-	-	<u>51.3</u>
AnySat	38.8	75.9	79.6	92.5	92.2	39.5
Galileo	40.4	-	-	-	-	39.5
SenPaMAE	40.7	59.9	79.5	89.5	78.3	39.3
DOFA	56.4	78.2	<u>80.4</u>	<u>92.8</u>	<u>96.3</u>	<u>51.3</u>
Panopticon	<u>59.3</u>	78.1	79.6	92.6	95.2	52.6

Table 10. GEO-Bench segmentation performance, mIoU. All values are percentages.

s	2	4	8	13
RGB MS	81.2	85.3	83.6	81.2

Table 11. Ablation of non-overlapping spectral crop size.